# Atomic collisions with relativistic heavy ions. VI. Radiative processes

R. Anholt, Ch. Stoller, J. D. Molitoris, D. W. Spooner, E. Morenzoni,* S. A. Andriamonje,† and W. E. Meyerhof
*Department of Physics, Stanford University, Stanford, California 94305-2196*

H. Bowman, J.-S. Xu,‡ Z.-Z. Xu,‡ and J. O. Rasmussen
*Nuclear Sciences Division, Lawrence Berkeley Laboratories, The University of California, Berkeley, California 94720*

D. H. H. Hoffmann
*Gesellschaft für Schwerionenforschung, D-6100 Darmstadt 11, West Germany*
(Received 12 November 1985)

Besides characteristic target and projectile x rays, x-ray continua and radiative-electron-capture photons are seen in collisions with relativistic heavy ions ranging in energy from 82 to 422 MeV/amu and in atomic number from Xe to U. The angular distribution, centroid energy, cross section, and line shape of the broad radiative-electron-capture lines are analyzed. The observed continua are due to primary- and secondary-electron bremsstrahlung. In the projectile frame, primary bremsstrahlung is the radiative scattering of incident target electrons from the projectile nucleus. The continuum cross sections and angular distributions are calculated, and are compared with experiment. Secondary-electron bremsstrahlung, due to the radiative scattering of ionized target electrons from other target nuclei, is target-thickness dependent, and the cross section increases roughly with the square of the target atomic number. The calculated primary-electron bremsstrahlung cross sections are lower than experiment.

## I. INTRODUCTION

In a previous paper in this series[1] (henceforth labeled I), we considered the emission of target $K$ and $L$ x rays in relativistic heavy-ion–atom collisions. Another paper in this series considers the relatively weaker projectile $K$ x-ray production.[2] However, the measured x-ray spectra also show a broad peak due to the radiative electron capture (REC) of target electrons into the projectile $K$ shell,[3–5] and an intense two-component continuum spectrum. When we began x-ray studies of relativistic ion-atom collisions using protons[6] and C ions,[7] we thought the continua were due to $\gamma$-ray production in nuclear reactions, and took little notice of them. With the use of very heavy ions, however, it became obvious that the continuum x-ray production cross sections, of the order of or greater than 100 b/[keV ($4\pi$ sr)] at some x-ray energies, were too large to be due to nuclear reactions. A nuclear reaction requires a close projectile-target nucleus encounter whose geometric cross section rarely exceeds a few barns, even for the heaviest projectiles. Therefore, nuclear reactions cannot produce $\gamma$ rays with such large cross sections. The continua must be due to atomic-physics phenomena.

Studies of molecular-orbital x rays in low-velocity ion-atom collisions[8] have long been concerned with the background bremsstrahlung continua due to nucleus-nucleus bremsstrahlung,[9] primary bremsstrahlung[10] (PB) (also called radiative ionization[11] or quasi-free-electron bremsstrahlung[12]), and secondary-electron bremsstrahlung[13,14] (SEB). In the present collisions where molecular orbitals are not formed, molecular-orbital x rays are absent. Furthermore, nucleus-nucleus bremsstrahlung is negligible (having a cross section of the order of or smaller than the nuclear reaction cross section). Therefore, the two continua most likely to be observed in relativistic heavy-ion–atom collisions are primary- and secondary-electron bremsstrahlung.

The study of these continua has a possible bearing on several issues. First, the cross sections show that in-beam spectroscopy of discrete low-energy nuclear $\gamma$ rays with high-$Z$ projectiles at relativistic velocities[15] is not possible unless one removes all background effects due to projectile and target electrons. Typical $\gamma$-ray production cross sections are less than 100 mb,[15] compared with a $\sim$100 b/keV background. Second, the data were particularly interesting to us because we had been interested in the mechanism for the production of and the magnitude of these continua at low projectile energies.[8] Their relative unobservability there made detailed examination impossible. At relativistic energies, somewhat different mechanisms come into play for forming these continua, but they can be studied under less hindered conditions. Finally, the possibility of using high-energy heavy ions to spark D-T fusion reactions[16] has brought a concern that the radiative preheating of the inner mechanical shells of high-gain inertial-fusion targets by projectile, target, and continuum x rays and the loss of energy from the pellets by x-ray emission might have deleterious effects on the energy-production efficiency.

We outlined most of the experimental methods used to obtain x-ray cross sections in paper I.[1] Therefore, only several minor modifications and special considerations applying to continuum x-ray measurements are discussed in Sec. II. The following three sections consider radiative electron capture (Sec. III), primary bremsstrahlung (Sec.

 

IV), and secondary-electron bremsstrahlung (Sec. V). Section VI discusses the $Z_t$ dependence of the latter two processes, and Sec. VII contains the conclusions.

## II. EXPERIMENT

Assuming that an electrical pulse with a relative amplitude of, e.g., 100 keV in the x-ray detector represents a detected 100-keV photon, one can calculate the double differential continuum cross section in units of b/[keV ($4\pi$ sr)] from the number of counts per channel in the x-ray spectrum as in Eqs. (1)—(3) of I. The only difference is the inclusion of a factor from the x-ray energy calibration (obtained using radioactive x-ray and $\gamma$-ray sources) converting the number of counts per channel to the number of counts per keV. In the spectra shown in this paper, small corrections for x-ray self-absorption in the target were not made to the measured cross sections, but were made to the theoretical cross sections. The conversion of every x-ray spectrum to cross-section spectrum proved useful to obtain integrated cross sections, especially for the broad REC peak where the detector efficiency varies over the physical width of the peak.

Near high-energy accelerators, there is always the danger that pulses in a photon detector are due to particles. Proof of the photon origin of the pulses seen in the x-ray detector was obtained by studying the attenuation of the continua in some cases, using 2- to 3-g/cm$^2$ Be and 0.533-g/cm$^2$ Mo absorbers. The Be absorber is sufficiently thick to prevent charged particles such as secondary electrons, scattered projectiles, and most heavy nuclear reaction products from reaching the x-ray detector. The Be absorber attenuates the x-ray photons negligibly, so the identity between a spectrum with the Be absorber and the unabsorbed spectrum corrected for Be absorption disqualifies the possibility that the spectrum is due to charged particles. With the Mo absorber, 50—150-keV x rays are attenuated by factors of 0.1—0.5. The identity between the absorbed spectrum and the corrected unabsorbed spectrum indicates that single photons of the measured energy are observed in the x-ray detector.

Figure 1 shows the importance of blocking secondary electrons using 3-g/cm$^2$ Be absorbers in 422-MeV/amu U + Ni collisions. At these projectile energies, secondary electrons with energies up to a classical end point $T_{\max}=2\gamma^2\beta^2mc^2=1183$ keV can be made. Due to electron multiple scattering in our thick targets, the electron spectrum at any detector angle should extend up to 1183 keV minus any energy lost by the electron penetrating the chamber window, 20 cm of air, and 500-$\mu$m Al and 250-$\mu$m Be windows on the Ge($i$) x-ray detector. This energy loss is about 300 keV for 1183-keV electrons, so the detected energy spectrum extends up to about $T'_{\max}=900$ keV in 422-MeV/amu U + Ni collisions. Quantum-mechanical considerations governing target electron ionization allow electron energies larger than $T_{\max}$, and the spectrum indeed extends above $T'_{\max}$. The Be absorber blocks these electrons without making too many additional electron bremsstrahlung photons, so the spectrum with a Be absorber extends only up to $\sim$300 keV, and represents detected photons. In future nuclear- and

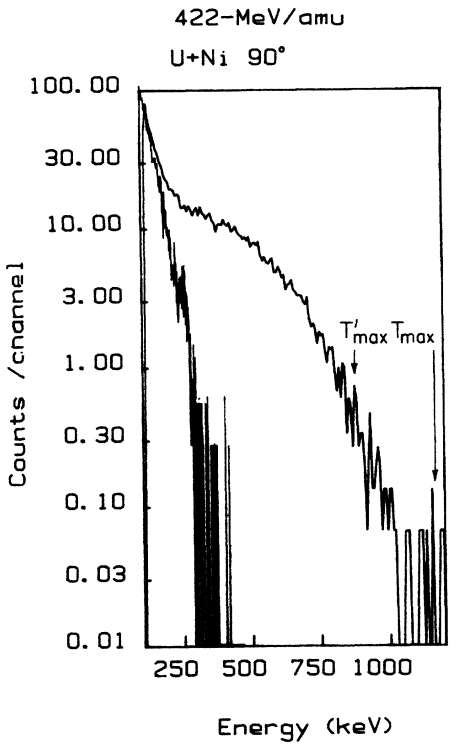


FIG. 1. Spectrum of pulses in an intrinsic Ge x-ray detector seen in 422-MeV/amu U + Ni collisions. The spectrum taken using a 3-g/cm$^2$ Be absorber blocking secondary electrons (thin line) ends near 300 keV, but the spectrum without an absorber (thick line) ends near the maximum secondary-electron energy $T'_{\max}$.

atomic-physics experiments using heavy ions with energies such as 10 GeV/amu, secondary electrons with energies greater than 138 MeV can be made, so that keeping electrons away from photon and baryon detectors can be a major difficulty.

The real pile-up process discussed in I can give additional unwanted contributions to the x-ray continuum spectra. In some of the targets used in this work, a single projectile can excite as many as 70 x-ray photons, and the relative probability that two photons simultaneously strike the x-ray detector giving a single larger pulse can be as large as several percent.[1] One normally observes discrete peaks due to the pile-up of two target $K\alpha$ photons or a $K\alpha$ and a $K\beta$ photon, but the $K\alpha$ and $K\beta$ photons can pile up on the continuum spectrum as well, giving a spurious continuum cross section at high x-ray energies. We define $dP/dE_x$ as the probability per projectile for detecting a photon of energy $E_x$ emitted from the target

$$\frac{dP}{dE_x}=n_2\frac{d^2\sigma}{dE_x\,d\Omega_x}TL\epsilon\Omega_x\,, \tag{1}$$

where $n_2$ is the target-atom density, $T$ is the target thickness traversed by the projectile, $L$ is the target x-ray self-absorption correction factor [Eq. (2) of I], $\epsilon\Omega_x$ is the x-ray detection probability, and $d^2\sigma/dE_x\,d\Omega_x$ is the absolute photon production cross section. For simplicity, we omit the differential in solid angle on the left-hand side of Eq.

(1). The pile-up spectrum is given by the product of probabilities:

$$\frac{dP''(E_T)}{dE_x} = \int_0^{E_T} dE_x \frac{dP(E_x)}{dE_x} \frac{dP(E_T - E_x)}{dE_x} , \quad (2)$$

and to first order in the pile-up correction, the measured spectrum is given by

$$\frac{dP'}{dE_x} = \frac{dP}{dE_x} + \frac{dP''}{dE_x} . \quad (3)$$

Figure 2 shows a calculated pile-up spectrum for 197-MeV/amu Xe + Ta collisions (see also Fig. 5 of I). Initially, the probability $dP/dE_x$ is not known; only the measured one, $dP'/dE_x$, is. We use the measured probability to calculate the pile-up spectrum. Conceivably, one can iteratively solve for the absolute probability, but we have not done this. We have used these calculations to determine where the pile-up process is negligible, and to make small corrections where necessary. In general, pile-up is negligible in the thinnest targets, and in the low-$Z$ targets where the target $K$ x rays (having the largest cross sections) are not observed. In the Xe + Ta spectrum shown in Fig. 2, the $K\alpha$ and $K\beta$ x-ray pile up occurs at the position expected for the REC peak, making REC unobservable there.

The second possible unwanted background comes from x-ray Compton scattering. A ~100-keV photon emerging from the target may Compton scatter and deposit a lower-energy pulse in the x-ray detector by (a) backscattering from other target atoms, (b) scattering from the chamber walls, (c) forward scattering on the absorber or collimator on the front face of the x-ray detector, (d) backscattering from the cold finger behind the detector, (e) scattering and escaping from the Ge detector material itself, or (f) scattering from anywhere else in the experimental area. A typical Compton scattering spectrum for the 81-keV $\gamma$-ray line in $^{133}$Ba placed at the target position is seen in Fig. 3. The Compton spectrum is far less intense than the sharp $\gamma$-ray line. Nevertheless, this scattering is important below the $K$-REC lines in the present spectra. The REC lines are much broader than the 81-keV line, but the Compton continuum spectrum below the REC lines is not broadened, so the REC peak height to Compton ratio is lower. The direct measurement of the Compton scattering intensity is difficult. Where separated $\gamma$-ray lines are available (e.g., 81 keV in $^{133}$Ba and 122 keV in $^{57}$Co), spectra taken with the radioactive sources measure processes (b)—(f) above; they cannot measure backscattering from the target material, and irrelevant backscattering from the source material is present. At low photon energies where photoelectric absorption dominates over Compton scattering, the Compton continuum is negligible.

Finally, there are small contributions from room $\gamma$-ray background and beam-induced nuclear $\gamma$-ray background from the Si particle detectors, which are dominant at high photon energies. This background was observed in measurements with no target, and prevents the use of targets

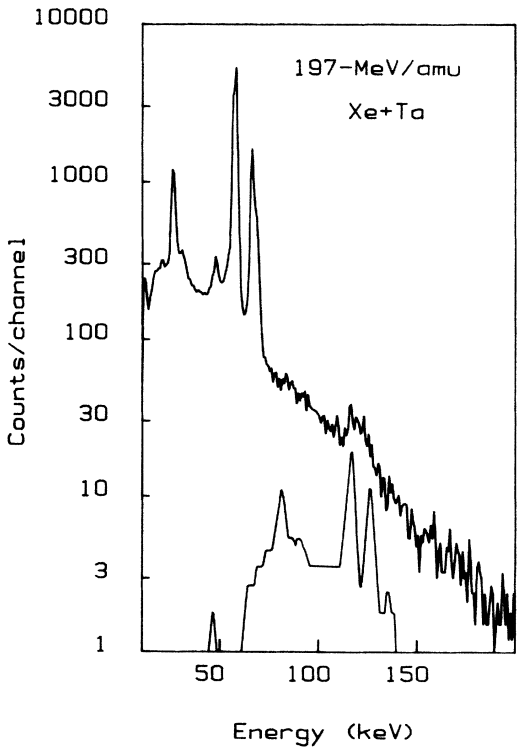


FIG. 2. X-ray spectrum in 197-MeV/amu Xe + Ta collisions using a thin Ta target. The lower curve shows the calculated pile-up spectrum $dP''/dE_x$.

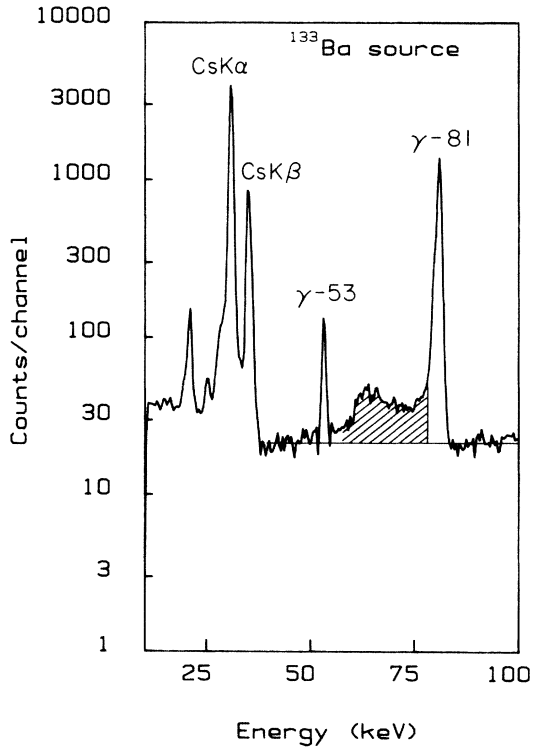


FIG. 3. $\gamma$-ray calibration spectrum showing the Compton scattering of $\gamma$ rays below the 81-keV $\gamma$ ray (cross-hatched area). The relatively flat background in this spectrum is due to the Compton scattering of high-energy $\gamma$ rays and electron-capture bremsstrahlung.

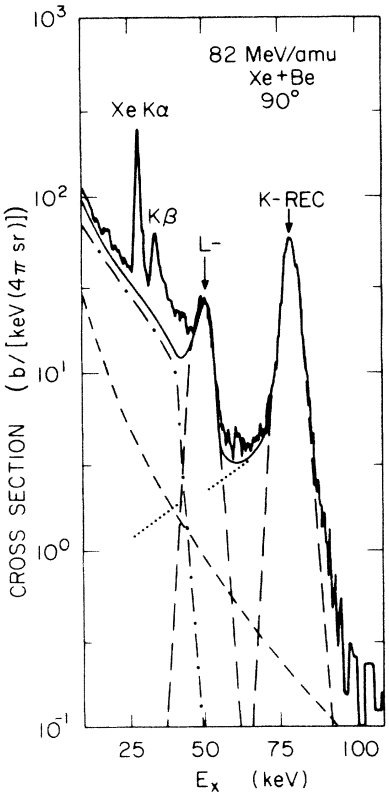


FIG. 4. Double-differential x-ray production cross sections seen in 82-MeV/amu Xe + Be collisions at a laboratory angle $\theta' = 90°$. Short-dashed line, secondary-electron bremsstrahlung; long-dashed line, radiative electron capture; dot-dashed curve, primary bremsstrahlung; dotted curves, estimated Compton scattering contributions; solid curve, total intensity.

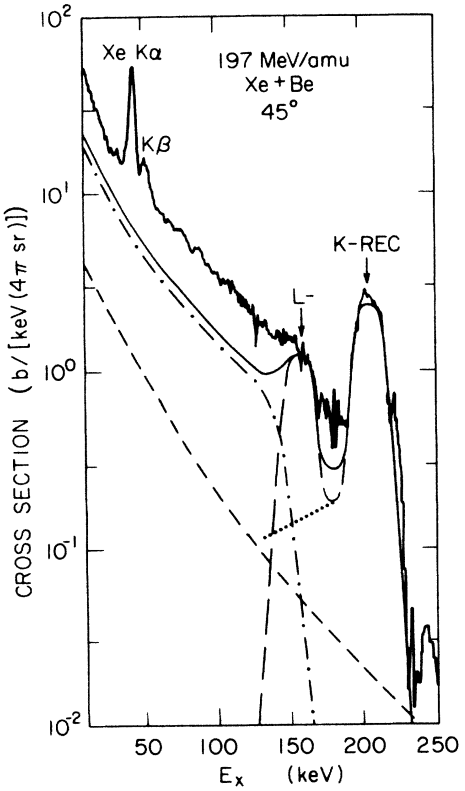


FIG. 6. Same as Fig. 4 for 197-MeV/amu Xe + Be at 45°.

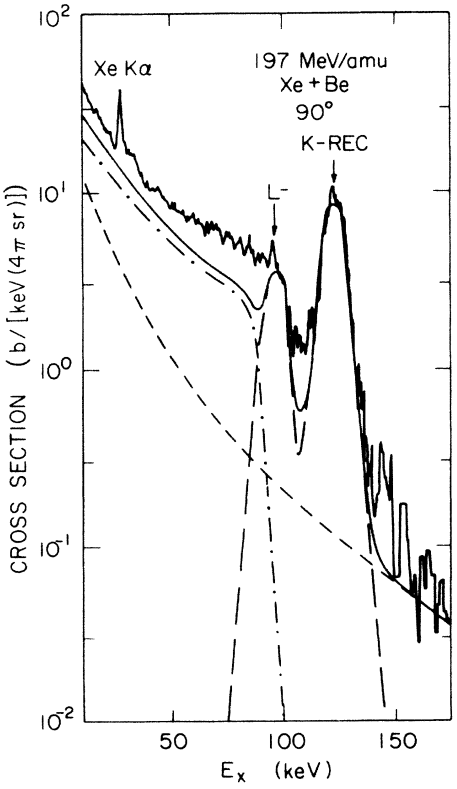


FIG. 5. Same as Fig. 4 for 197-MeV/amu Xe + Be at 90°.

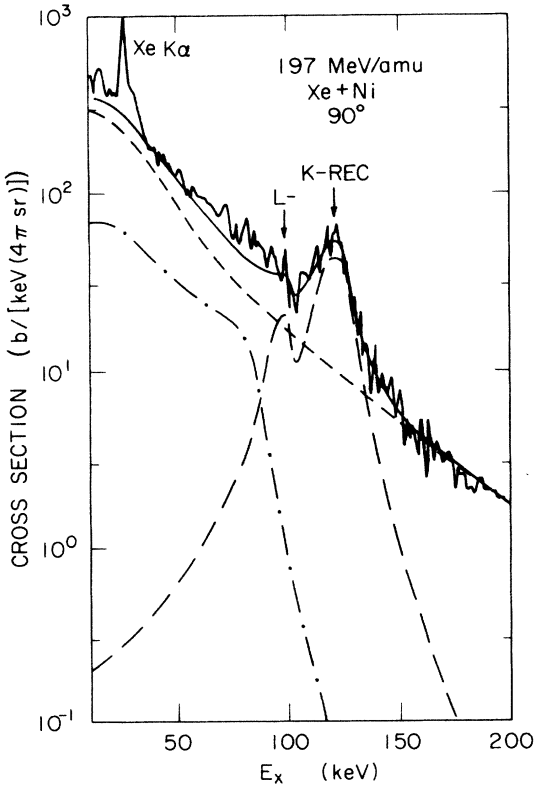


FIG. 7. Same as Fig. 4 for 197-MeV/amu Xe + Ni at 90°.

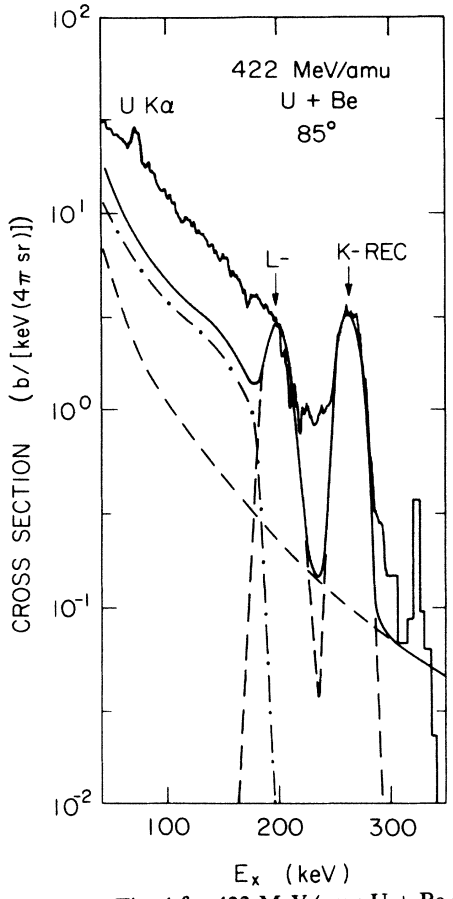


FIG. 8. Same as Fig. 4 for 422-MeV/amu U + Be at 90°.

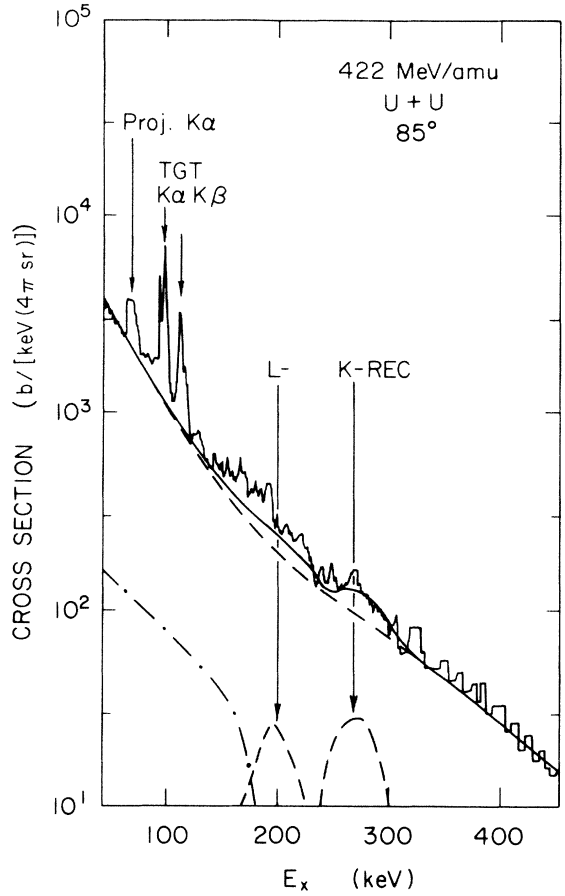


FIG. 9. Same as Fig. 4 for 422-MeV/amu U + U at 90°.

thinner than $\sim 1$ mg/cm$^2$. We subtracted a no-target background spectrum from most of the data.

Figures 4—9 show spectra from several different collisions. In order of decreasing prominence, the spectra show target $K$ x rays, projectile $K$ x rays, REC, PB, and SEB. Target $K$ x rays are seen in U + U collisions, but not in the Ge detector in the lighter-$Z$ targets. The projectile $K\alpha$ and $K\beta$ x rays are seen in most spectra. They are Doppler shifted (compare 197-MeV/amu Xe + Be at 45° and 90°; Figs. 5 and 6), and are Doppler broadened, which is clearly seen in the U projectile $K\alpha$ line in U + U collisions (Fig. 9). The $K$-REC peak varies in x-ray energy with the beam energy (from $\sim 80$ keV in 82-MeV/amu Xe + Be collisions to $\sim 260$ keV in 422-MeV/amu U + Be collisions at 90°), and is Doppler shifted with the detection angle (compare 197-MeV/amu Xe + Be at 45° and 90°). The REC peak is relatively less intense than the continua in the high-$Z_t$ Xe + Ni collisions than in the low-$Z_t$ Xe + Be collisions, but the absolute intensity is greater. A smaller peak due to $L$ REC (capture of target electrons into the projectile $L$ shell) is weakly seen in all spectra, but is most intense in 82-MeV/amu Xe + Be collisions (Fig. 4). The continuum spectrum ending below the $L$-REC line is due to PB, and is most easily seen in the Be target spectra. The PB end-point energy Doppler shifts like the REC centroid energy, as seen at 45° and 90° in 197-MeV/amu Xe + Be collisions. REC and PB disappear in the high-$Z_t$ targets, and a continuum due to SEB having no apparent end point (over these ranges of photon energies) is present. The intensity of this continuum increases faster with $Z_t$ than the PB or REC intensities.

These qualitative remarks summarize the angular, $Z_t$, and x-ray-energy dependences of REC, PB, and SEB. The following sections discuss the quantitative analysis of these spectra.

## III. RADIATIVE ELECTRON CAPTURE

### A. The centroid energy

In the laboratory (primed coordinates), the $K$-REC centroid energy is given by

$$E'_{K\,\mathrm{REC}}=\gamma^{-1}[(\gamma-1)mc^2+E_K](1-\beta\cos\theta')^{-1}\,, \qquad (4)$$

where $\beta$ is ion velocity relative to the speed of light $c$, $\gamma^{-2}=1-\beta^2$, and $E_K$ is the projectile $K$-shell binding energy. The binding energy of the captured target electron is neglected in this formula. The projectile $K$ binding energy is uncertain because the projectile initially has between 0 and 1 $K$ electron, so one should use either the H-like or He-like binding energy. The Dirac H-like binding energy is given by[17]

$$E_K(\mathrm{H})=[1-(1-\alpha^2 Z_p^2)^{1/2}]mc^2 , \quad (5)$$

where $\alpha^{-1}=137.037$. The difference between nonrelativistic H-like and He-like $K$-shell binding energies is given by

$$E_K(\mathrm{He})-E_K(\mathrm{H})=0.315-\tfrac{5}{4}Z_p \text{ Ry} , \quad (6)$$

which is approximately 0.9 keV for Xe and 1.8 keV for U.

The most uncertain quantity in Eq. (4) is the beam velocity, which is not known after passing through several materials to within $\sim 10$ MeV/amu for very heavy ions. Instead of comparing the measured REC centroids with calculations, we fitted the centroids to Eq. (4), and solved for the beam velocity or energy, as shown in Table I. The uncertainty in the centroid energy gives an uncertainty in the beam energy of approximately 1–2%, which is approximately equal to the difference between calculations using the H-like and He-like $E_K$ values. We do not understand the difference between the quoted BEVALAC energy (in which allowance has been made for known energy degradation upstream of the target), and the ones obtained from the REC peak. Averages of the H-like and He-like REC values were adopted.

### B. The REC angular distribution

We discussed the $K$-REC photon angular distribution in a previous paper,[5] where we showed, using a simplified formula for the photoelectron angular distribution for the inverse process, that there is a cancellation of the electron retardation factor and the Lorentz transformation factor when the photoelectric angular distribution is transformed from the projectile to the laboratory frame. As a consequence, the photon angular distribution varies approximately as $\sin^2\theta'$, where $\theta'$ is the laboratory angle between the beam and photon directions.[4] Corrections to this distribution, obtained when the Sauter formula[18,19] or Dirac electronic wave function[20] are used to calculate the photoelectric angular distribution, are smaller than $\pm 15\%$, and are difficult to measure.

Measurements of the angular distribution of $L$ REC (capture into the projectile $L$ shells) would be interesting since the component due to $2p$ capture has a different photoelectric angular distribution than the $1s$ and $2s$ capture components.[17] Unfortunately, separating the $L$ REC intensity from the PB and SEB backgrounds is not possible presently. We measured the $K$-REC angular distribution for several angles in 175-MeV/amu La + Be, 82-MeV/amu Xe + Be, and 422-MeV/amu U + Be collisions and found results approximately consistent with $\sin^2\theta'$ in all cases.

### C. REC cross sections

For a $\sin^2\theta'$ laboratory angular distribution, the total $K$-REC cross section is given by

$$\sigma_{K\,\mathrm{REC}}=\tfrac{2}{3}\int dE_x' \frac{d^2\sigma(\theta'=90°,E_x')}{dE_x'\,d\Omega_x'} , \quad (7)$$

where the cross section has the units of b/[keV ($4\pi$ sr)], and the integration extends over the $K$-REC peak area. The integrated $K$-REC cross sections were given in previous papers,[2,5] where they were applied to the determination of the number of projectile $K$ vacancies inside solid targets.

In Ref. 5 the $K$-REC cross sections were calculated from the $K$-shell Dirac photoelectric cross sections. Several other calculations of the $K$-shell photoelectric cross section could be used: (1) the Bethe-Salpeter formula [Eq. (7.7) of Ref. 17] valid for nonrelativistic, one-electron $1s$ and continuum wave functions, (2) the Sauter formula,[19] or (3) the many-electron values, calculated using relativistic Hartree-Slater wave functions.[21] For the zero- to two-electron high-$Z_p$ projectiles used, Dirac wave functions are most appropriate,[20] but the Dirac and Hartree-Slater $K$-shell photoelectric cross sections differ by less than 4% in relevant region of photon energy and $Z_p$. As Table II shows, all theories predict similar REC cross sections for 200-MeV/amu collisions with fully stripped projectiles. At lower beam velocities, the Sauter formula underestimates the cross section. For high-$Z_p$ and high-velocity projectiles, the Bethe-Salpeter formula[17] seems to be inferior.

### D. The REC line shape

For stationary target electrons, the REC line shape is very sharp at the x-ray energy $(\gamma-1)mc^2+E_K$ in the projectile frame. In fact, the electrons in each shell $s$ have a binding energy $E_s$ and a momentum $\mathbf{p}_s$ which adds vectorially to the projectile momentum $\mathbf{p}=\gamma\beta mc$ so that the x-ray energy in the projectile frame (unprimed coordinates) is given by[3]

$$E_x=(\gamma-1)mc^2+E_K-E_s+\gamma\beta c p_{sz} , \quad (8)$$

TABLE I. $K$-shell binding and projectile energies from REC centroids.

| Beam | $E_K$(H) (keV) | $E_K$(He) (keV) | $E_p$(H-like) (MeV/amu) | $E_p$(He-like) (MeV/amu) | Adopted (MeV/amu) |
|---|---|---|---|---|---|
| "180-MeV/amu Xe" | 41.3 | 40.4 | 196±3 | 198±3 | 197 |
| "80-MeV/amu Xe" | 41.3 | 40.4 | 81±1.6 | 83±1.2 | 82 |
| "170-MeV/amu La" | 46.3 | 45.1 | 173±4 | 176±4 | 175 |
| "400-MeV/amu U" | 132.2 | 130.6 | 422±8 | 429±8 | 422 |

TABLE II. Radiative-electron-capture cross sections into the $K$ shell (barns).

| | Sauter | Bethe[a] | HS[b] | Dirac |
|---|---|---|---|---|
| 82-MeV/amu Xe | 36 | 80 | 80 | 83 |
| 197-MeV/amu Xe | 22 | 19 | 20 | 21 |
| 175-MeV/amu La | 28 | 28 | 29 | 30 |
| 422-MeV/amu U | 44 | 28 | 37 | 38 |

[a]Reference 17.
[b]Hartree-Slater (Ref. 21).

where $p_{sz}$ is the component of the electron momentum along $\hat{\beta}$. To obtain the cross section for emission of REC photons with energy $E_x$, the total REC cross section is weighted by the probability for the electron to have the momentum $p_{sz}$, which is the Compton distribution $J_s$ for shell $s$:[3]

$$\frac{d^2\sigma(\theta,E_x)}{d\Omega\, dE_x}=\sum_s \frac{1}{\hbar\gamma\beta c}\left[\frac{d\sigma_{\rm REC}}{d\Omega}\right]_{p+p_{sz}} J_s(p_{sz})\ . \tag{9}$$

We made calculations using the individual-shell Compton distributions[22] for Xe + Au, Zr, and Be collisions, and found that after folding in Doppler broadening, one can neglect the electron binding energy $E_s$ in Eq. (8) for the observable part of the REC spectrum. Hence, one can use the total Compton distribution $J(p_z)$ in Eq. (9):

$$\frac{d^2\sigma}{d\Omega\, dE_x}=\frac{1}{\hbar\gamma\beta c}\left[\frac{d\sigma_{\rm REC}}{d\Omega}\right]_{p+p_z} J(p_z)\ . \tag{10}$$

The observed REC lines are much broader than the impulse-approximation predictions, due to the Doppler-shift spread of the REC photons over the angles subtended by the x-ray detector. Our 1000-mm$^2$ Ge($i$) x-ray detector located 24 cm away from the target subtended approximately 8° in the laboratory, giving a Doppler width

$$\Delta E'_x=E'_x\beta\sin\theta'(1-\beta\cos\theta')^{-1}\Delta\theta'\ , \tag{11}$$

equal to 8 keV for 197-MeV/amu ions at $\theta'=90°$. In fact, the spread is larger than this, since the beam spot on the target seen from the center of the x-ray detector subtended $\sim 5°$, giving a total range of angles approximately equal to 13°. To obtain the Doppler-broadened line shape, we averaged over all angles subtended by the x-ray detector, weighted by the geometrical probability for each angle.

Also included in calculations of the REC line shape are contributions from capture into the projectile $L$ shell and outer shells. The relative capture cross sections were taken from relativistic Hartree-Slater photoelectric cross sections.[21] According to the bound-state normalization theory of Pratt,[23] the many-electron $L$ and outer-shell photoelectric cross sections are reduced by screening factors, which are the ratio of the many-electron electronic density at the origin to the Dirac value. As we require Dirac photoelectric cross sections, for which tabulations are not as easy to obtain as many-electron ones, we divided the Hartree-Slater $L$ and outer-shell cross sections by screening factors calculated by Schmickley.[24] This should give Dirac photoelectric and therefore REC cross sections accurate to about ±5%. Capture into the projectile $L$ shell goes mostly into the $2s$ orbital so we used the Dirac $2s$ binding energy to calculate the $L$-REC line centroid. For all other shells, we used one-half of the $2s$ binding energy.

Figures 4–9 compare measured and calculated REC line shapes, normalized to the total measured peak $K$-REC cross section. The observed linewidths are due mostly to Doppler broadening; little can be learned about Compton distributions from these measurements. One could reduce the Doppler broadening by using Soller slits on the x-ray detector, but we emphasized cross-section determinations in this work, which are more difficult to obtain when Soller slits are used. Slightly wider calculated REC line shapes in the high-$Z_t$ targets are obtained, due to the larger width of the Compton distribution, but these line shapes are more difficult to observe experimentally because of the high SEB background. We did not find it possible to explain the entire intensity just below the $K$-REC line in the Be-target spectra where SEB and PB play an insignificant role. At 82 MeV/amu, most of this intensity is due to Compton scattering of the $K$-REC photons (as determined using the 81-keV $\gamma$-ray line), but at 197 MeV/amu at 90°, a less significant part is due to Compton scattering (calibrated with the 122-keV $\gamma$-ray line in $^{57}$Co). The Compton scattering contribution cannot be ascertained in the U + Be and Xe + Be (45°) spectra.

The 197-MeV/amu Xe + Be spectrum at 90° (Fig. 5) differs from one published earlier[5] in the relative $K$ to outer-shell REC ratios. Part of this is due to the application of screening factors to the outer-shell REC cross sections. In addition, the outer-shell REC is enhanced over the $K$ REC because the presence of projectile $K$ electrons blocks $K$ REC, but not outer-shell REC. This is especially seen in U + Be collisions, where 1.4 projectile $K$ electrons are present on the average.[5] This reduces the $K$-REC cross section by a factor of 0.3, so the relative outer-shell to $K$-REC cross section ratio is closer to unity than to 0.4, the ratio for bare projectiles.

## IV. PRIMARY BREMSSTRAHLUNG

### A. Cross sections

Radiative electron capture is the capture of target electrons into bound states of the projectile. An analogous process is the capture into continuum states of the projectile, called primary bremsstrahlung. Viewed differently: in the projectile frame, the projectile nucleus is bombarded by target electrons with mean kinetic energy $(\gamma-1)mc^2$. These may emit bremsstrahlung photons with energy $E_x$ as large as the electron kinetic energy in the projectile frame. In the laboratory frame, the end-point x-ray energy is given by

$$E'_x=(\gamma-1)mc^2\gamma^{-1}(1-\beta\cos\theta')^{-1}\ , \tag{12}$$

which varies in 197-MeV/amu Xe + Be collisions from approximately 88 keV at 90° (Fig. 5) to 147 keV at 45° (Fig. 6).

As a first approximation, the PB cross section is just the bremsstrahlung cross section for $Z_t$ electrons with kinetic energy $T=(\gamma-1)mc^2$ bombarding the projectile nucleus, Lorentz transformed into the laboratory frame:[4,12]

$$\frac{d^2\sigma_{\rm PB}(E'_x,\theta')}{dE'_x d\Omega'}=Z_t\frac{d^2\sigma_{\rm brem}(E_x,\theta,Z_p,T)}{dE_x d\Omega}\frac{dE_x}{dE'_x}\frac{d\Omega}{d\Omega'}\ , \tag{13}$$

where

$$\cos\theta=\frac{\beta-\cos\theta'}{1-\beta\cos\theta'}\ ,\quad \frac{d\Omega}{d\Omega'}=\frac{1-\beta^2}{(1-\beta\cos\theta')^2}\ ,$$

and

$$\frac{dE_x}{dE'_x}=\frac{1-\beta\cos\theta'}{(1-\beta^2)^{1/2}}\ . \tag{14}$$

Here the unprimed quantities are projectile-frame (center-of-mass for projectile-electron collisions) quantities, and the primed ones are laboratory-frame ones. For the bremsstrahlung cross section we used the Bethe-Heitler formula including the Elwert correction factor [Eq. (2BN) of Ref. 25].

Equations (12)—(14) assume the target electrons are free and have no intrinsic momentum, and therefore give a sharp cutoff where the x-ray center-of-mass energy is equal to the electron kinetic energy. When one adds the Fermi momentum of the target electrons $\mathbf{p}_s$ to the translational momentum $\mathbf{p}=\gamma\beta mc$, larger electron kinetic energies and end-point energies are obtainable. The continuum shape can be calculated in the impulse approximation using[11]

$$\frac{d^2\sigma_{\rm PB}}{dE'_x\,d\Omega'}=\int_{-\infty}^{+\infty}dp_z\,J(p_z)\frac{d^2\sigma_{\rm PB}(T,E'_x,\theta')}{dE'_x d\Omega'}\ , \tag{15}$$

where the PB cross section on the right-hand side is given by Eq. (13), $J(p_z)$ is the Compton profile,[22] the binding energy of the target electrons in each shell is neglected as for REC, and the electron kinetic energy is given by

$$T=\{[(\gamma\beta+p_z/mc)^2+1]^{1/2}-1\}mc^2\ . \tag{16}$$

Finally, we average over the laboratory angles subtended by the x-ray detector. These folding procedures have no effect on the PB cross section for x-ray energies well below the end point. The electron momentum folding causes the spectrum to drop off more slowly above the end point; the Doppler folding shifts the position of the end point to slightly higher energies, due to the inclusion of smaller laboratory angles, and rounds off the continuum shape near the end point.

The calculated PB cross sections are generally lower than experiment, as discussed in more detail below. However, the shape of the continua agree well with experiment, at least where PB is not obscured by SEB, as seen in the Be-target spectra.

### B. The angular distribution of PB

The bremsstrahlung cross section has an approximate angular distribution in the center-of-mass frame of the form[26]

$$\frac{d^2\sigma_{\rm brem}}{dE_x d\Omega}=\frac{\sin^2\theta+\frac{1}{2}-[3\beta/(1+\beta^2)]\cos\theta}{(1-\beta\cos\theta)^4}\ , \tag{17}$$

where $\theta$ here is the angle between the electron direction and photon direction, so the angular distribution is peaked backwards in the laboratory. If we neglect all but the $\sin^2\theta$ term in this expression, we get a bremsstrahlung angular distribution that is identical in form to the photoelectron angular distribution determining REC, hence, almost like REC, the angular distribution of PB in the laboratory is of the form

$$\frac{d^2\sigma_{\rm PB}(E'_x,\theta')}{dE'_x d\Omega'}\sim\sin^2\theta'(1-\beta\cos\theta')\ . \tag{18}$$

Unlike for REC, the PB cross section is differential in a laboratory x-ray energy, so instead of obtaining an angular distribution proportional to $\sin^2\theta'$, an additional term $1-\beta\cos\theta'$ is present. The angular distribution is determined keeping the center-of-mass x-ray energy $E_x$ constant. As an example, for $E_x=45$ keV in 197-MeV/amu Xe + Be collisions, the continuum cross sections must be measured at $E'_x=62$ keV at 45°, 37 keV at 90°, 27 keV at 135°, etc. Figure 10 shows that the measured angular distributions are indeed peaked at backward angles, as suggested by Eq. (18). The solid lines were calculated with the Bethe-Heitler formula for the bremsstrahlung angular distribution, normalized to the data near $\theta'=90°$. Some pieces of data are missing because the laboratory energy is below the detector threshold. Where needed, we have extrapolated the continuum cross section beneath the Xe $K\alpha$ lines. The agreement between the measured and calculated PB angular distribution shapes is very good.

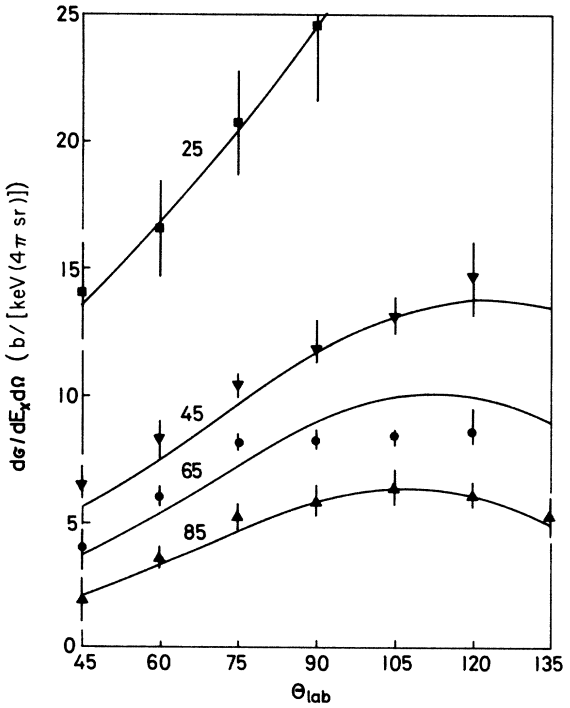


FIG. 10. Angular distribution of radiation in 197-MeV/amu Xe + Be collisions compared with the Bethe-Heitler calculations of primary bremsstrahlung, normalized at $\theta'=90°$. The numbers give the center-of-mass photon energy in keV.

## V. SECONDARY-ELECTRON BREMSSTRAHLUNG

In a binary collision between a 197-MeV/amu heavy ion and a nearly free electron, electrons with kinetic energies up to 450 keV can be produced. These electrons can collide with other nearby target nuclei in solid targets, emitting SEB photons with energies up to ~450 keV. To calculate the cross section for SEB, we assume (i) that $Z_t$ target electrons are free and scatter elastically from the projectile nucleus, and (ii) the ionized electrons follow a tortuous path inside the solid target so electrons never leave the target material, and the angle between the bremsstrahlung photon direction and the projectile direction is random. The latter assumption follows from a calculation[27] of the mean multiple-scattering angle for 50–200-keV electrons in the 5–50-mg/cm$^2$ targets used. The mean multiple-scattering angle is of the order of several radians, so one cannot assume the electrons travel in a straight line after being emitted. With these assumptions, the cross section is given by

$$\frac{d\sigma_{\rm SEB}(E'_x)}{dE'_x} = Z_t \int_{E'_x}^{E_{\max}} dE'_e \frac{d\sigma_{\rm elas}}{dE'_e} \int_{E_e}^{E'_x} -\frac{dE'_e}{S(E'_e)} n_2 \frac{d\sigma_{\rm brem}(E'_x)}{dE'_x} , \tag{19}$$

where the elastic electron scattering cross section is given by the McKinley-Feshbach equation[28]

$$\frac{d\sigma_{\rm elas}}{dE_e} = 2\pi \frac{(Z_p e^2)^2}{mc^2\beta^2} \frac{1}{E_e^2} \times \left\{ 1 - \frac{\beta^2 E_e}{E_{\max}} + \pi Z_p \alpha\beta \left[ \left[ \frac{E_e}{E_{\max}} \right]^{1/2} - \frac{E_e}{E_{\max}} \right] \right\} , \tag{20}$$

$E_{\max} = 2\gamma^2\beta^2 mc^2$, $S(E_e)$ is the electron stopping power in the target material given by

$$S(E_e) = \frac{4\pi e^4 n_2}{mc^2\beta_e^2} Z_t \left[ \ln \left[ \frac{2\gamma_e^2\beta_e^2 mc^2}{\langle I \rangle} \right] - \beta_e^2 \right] , \tag{21}$$

$\langle I \rangle$ is the average ionization potential,[29] $\gamma_e = 1 + E'_e/mc^2$, $\beta_e^2 = 1 - \gamma_e^{-2}$, and $d\sigma_{\rm brem}/dE_x$ is the angle-integrated bremsstrahlung cross section calculated using the Bethe-Heitler-Elwert formula [Ref. 25, Eq. (3BN)].

SEB is dominant for high-$Z_t$ targets where the agreement between theory and experiment is very good (Fig. 9 for U + U collisions). In earlier calculations[5] where we assumed the ionized electron travels in a straight line, and can leave the target, the theoretical calculations fell factors of 0.2–0.5 below experiment. We attempted to verify the assumed isotropic angular distribution, but for technical reasons, the measurement failed.

## VI. DISCUSSION

For SEB, the bremsstrahlung cross section in Eq. (19) varies as $Z_t^2$, the stopping power $S(E)$ as $Z_t/A_t$, where $A_t$ is the target mass number, $n_2$ varies as $A_t^{-1}$, the elastic cross section varies as $Z_p^2$, and $Z_t$ electrons can participate in SEB, so the SEB cross section for infinite target thickness varies as $Z_p^2 Z_t^2$. For PB, the bremsstrahlung cross section varies as $Z_p^2$ and $Z_t$ electrons participate, so the PB cross section varies as $Z_p^2 Z_t$.

Figure 11 shows the $Z_t$ dependence of continuum x-ray production in 82-, 197-, and 422-MeV/amu Xe and U collisions. The laboratory x-ray energy chosen falls within the region where both PB and SEB are present. Given the good agreement between the shape of the calculated and measured x-ray spectra, identical qualitative results are expected at other x-ray energies. The x-ray energies were chosen to avoid as much as possible interference with characteristic x rays and REC (though cross sections for continua falling beneath target x-ray lines could not be obtained at some $Z_t$ values).

The fully logarithmic plot in Fig. 11 demonstrates that PB increases linearly with $Z_t$ and SEB increases quadratically with $Z_t$. Good agreement between the SEB calculations and experiment is found at high $Z_t$, but there is a systematic discrepancy at low $Z_t$ where PB dominates. If one subtracts the calculated SEB contribution from the measured cross sections, the resulting cross sections increase linearly with $Z_t$, as predicted by the PB theory, but are factors of 1.7 (197-MeV/amu Xe) to 2.9 (422-MeV/amu U) too high.

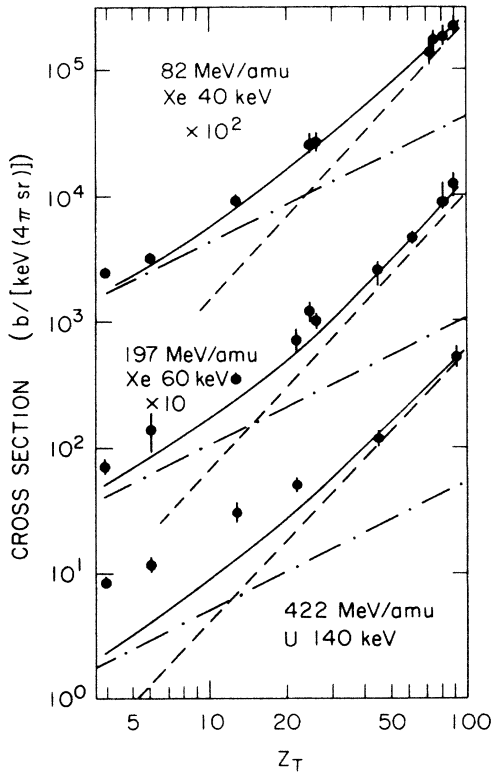


FIG. 11. Cross sections for continuum x-ray emission in 82-MeV/amu Xe collisions at laboratory x-ray energies of 40 keV, 197-MeV/amu Xe collisions at 60 keV, and 422-MeV/amu collisions at 140 keV against target atomic number. The short-dashed line shows the calculated secondary-electron bremsstrahlung yield, the dot-dashed curve shows primary bremsstrahlung, and the solid line shows the total bremsstrahlung intensity.

We have double checked every assumption made to determine PB and believe the calculated cross sections are accurate to within ±30% (see also the Appendix). Tseng *et al.*[26] and Lee *et al.*[30] compared double- and single-differential electron bremsstrahlung cross sections calculated with the Bethe-Heitler-Elwert formula, fully screened atomic electronic wave functions, and Dirac wave functions. For the present nearly bare projectiles, Dirac electronic wave functions should be used, but generally there is less than a ±30% difference between all three calculations in the relevant electron energy, $Z_p$, and angular range.

The SEB calculations are less certain that the PB ones, but we have not discovered a realistic assumption that would increase the SEB yield enough to explain the discrepancy between theory and experiment for the Be targets. In particular, one assumption is that a significant number of electrons escape from the Be target and collide with the Al ($Z_{\text{wall}}=13$) or Mylar ($Z_{\text{wall}}\sim 6.6$) chamber walls. The relative contribution from the chamber wall increases with $Z_{\text{wall}}$, not as $Z^2_{\text{wall}}$, because if the electron stops in the wall, one power of $Z$ is canceled. We made a few calculations for low-$Z_t$ targets assuming that the electrons travel in a straight line, then upon leaving the target collide with an Al wall and make SEB along the remaining part of their range. This upper limit to the wall contribution increases the 197-MeV/amu Xe + Be and U + Be SEB contributions by less than factors of 2, which cannot explain the discrepancy between theory and experiment in those cases.

## VII. CONCLUSIONS

We conclude that the disagreement between the theory of PB and experiment is fundamental. The shape of the PB spectrum and the angular distribution of the radiation agree with theory, but the magnitude of the measured cross sections differ by factors of 1.7–2.9. Given the reasonably good agreement between measurements of atomic-electron bremsstrahlung cross sections[31] for similar electron energy and $Z$ ranges and calculations of Kissel *et al.*[32], it is unlikely that the origin of the disagreement between the PB calculations and experiment lies in the electron bremsstrahlung cross sections. It should be emphasized, however, that electron bremsstrahlung cross sections have never been measured on bare, high-$Z$ ions, but all Dirac–many-electron bremsstrahlung cross-section comparisons suggest that little difference should exist. The discrepancy may indicate a failure of the impulse approximation to describe electron bremsstrahlung for incident projectiles on bound target electrons, but the good agreement between experiment and REC cross sections calculated with the same theory limits the options one has for modifying the impulse approximation. Possibly, high-$Z$ projectiles polarize the target atoms to such an extent that the density of target electrons increases near the projectile nucleus, but this should affect the PB and REC cross sections equally. Wake or bound electrons traveling with the projectile bombard target nuclei giving bremsstrahlung up to the PB end point, but given the lower bremsstrahlung cross sections on target nuclei such as Be, it is unlikely that wake-electron bremsstrahlung can compete with target-electron–projectile-nucleus bremsstrahlung.

The present measurements are not sufficient to ascertain whether the discrepancy between theory and experiment is a $Z_p$-dependent or velocity-dependent effect. The two measurements for Xe ions at 82- and 197-MeV/amu, where the ratio of experiment to theory varies from $1.7\pm0.2$ to $1.8\pm0.2$, are not sufficient to tell. Measurements with Xe and U ions up to 1000 MeV/amu or U ions down to 100 MeV/amu would be useful.

## ACKNOWLEDGMENTS

Discussions with H. Gould, E. Spindler, D. H. Jakubassa-Amundsen, F. Bell, and H.-D. Betz are greatly appreciated. This work was supported in part by the National Science Foundation Grant No. PHY-83-13676 and by the U.S. Department of Energy Contract No. DE-AC03-76SF00098.

## APPENDIX: CALCULATION OF PRIMARY BREMSSTRAHLUNG

As a check on the PB calculations using the Bethe-Heitler formula, one can also calculate PB using Eqs. (13) and (14) and tables of electron bremsstrahlung cross sections for neutral atoms given by Kissel *et al.*[32] Consider 197-MeV/amu Xe + Be collisions at 90°. The electron energy in the projectile frame is $T=107$ keV, so we use Kissel's tables for 100-keV electrons. The center-of-mass angle, $\theta=\cos^{-1}[(\beta-\cos\theta')/(1-\beta\cos\theta')]$, is 55°. For a center-of-mass x-ray energy of $0.5\times107$ keV (laboratory energy 44 keV), the bremsstralung cross section is

$$\frac{d^2\sigma_{\text{brem}}}{dE_x d\Omega}=4\pi S\times(\text{spectrum})\times\frac{Z_p^2}{\beta^2 E_x}$$

$$=1.9\ \text{b/[keV}\ (4\pi\ \text{sr})]\ ,$$

where $S=0.1388$ is the shape function and (spectrum) $=6.426$ mb is the reduced angular integrated cross section defined by Kissel *et al.*[32] Using Eq. (13), we get

$$\frac{d^2\sigma_{\text{PB}}}{dE'_x d\Omega'}=Z_t\frac{d^2\sigma_{\text{brem}}}{dE_x d\Omega}\frac{(1-\beta^2)^{1/2}}{1-\beta\cos\theta'}$$

$$=6.3\ \text{b/[keV}\ (4\pi\ \text{sr})]\ .$$

The Bethe-Heitler result is 5.9 b/[keV ($4\pi$ sr)] and the measured continuum cross section minus the SEB contribution is 9.0 b/[keV ($4\pi$ sr)].

*Permanent address: Swiss Institute for Nuclear Research, CH-5234 Villingen, Switzerland.

†Permanent address: Centre d'Etudes Nucléaires de Bordeaux–Gradignan, 33170 Gradignan, France.

‡Permanent address: Department of Physics, Fudan University, Shanghai, People's Republic of China.

[1]R. Anholt, W. E. Meyerhof, Ch. Stoller, E. Morenzoni, S. A. Andriamonje, J. D. Molitoris, D. H. H. Hoffmann, H. Bowman, J. S. Xu, Z. Z. Xu, D. Murphy, K. Frankel, K. Crowe, and J. O. Rasmussen, Phys. Rev. A **30**, 2234 (1984).

[2]R. Anholt and W. E. Meyerhof, Phys. Rev. A **33**, 1556 (1986).

[3]M. Kleber and D. H. Jakubassa, Nucl. Phys. **A252**, 152 (1975).

[4]E. Spindler, H.-D. Betz, and F. Bell, Phys. Rev. Lett. **42**, 832 (1979).

[5]R. Anholt, W. E. Meyerhof, Ch. Stoller, E. Morenzoni, S. A. Andriamonje, J. D. Molitoris, D. H. H. Hoffmann, H. Bowman, J. S. Xu, Z. Z. Xu, and J. O. Rasmussen, Phys. Rev. Lett. **53**, 234 (1984).

[6]R. Anholt, S. Nagamiya, H. Bowman, J. Ioannou, E. Rauscher, and J. O. Rasmussen, Phys. Rev. A **14**, 2103 (1976).

[7]R. Anholt, J. Ioannou, H. Bowman, E. Rauscher, S. Nagamiya, J. O. Rasmussen, T. Shibata, and H. Ejiri, Phys. Lett. **59A**, 429 (1977).

[8]R. Anholt, Rev. Mod. Phys. **57**, 995 (1985).

[9]J. Reinhardt, G. Soff, and W. Greiner, Z. Phys. A **276**, 285 (1976).

[10]H. W. Schnopper, J. P. Delvaille, K. Kalata, A. R. Sohval, M. Abdulwahab, K. W. Jones, and H. E. Wegner, Phys. Lett. **47A**, 61 (1974).

[11]D. H. Jakubassa and M. Kleber, Z. Phys. A **273**, 23 (1975).

[12]A. Yamadera, K. Ishii, K. Sera, M. Sebata, and S. Morita, Phys. Rev. A **23**, 24 (1981).

[13]F. Folkmann, C. Gaarde, T. Huus, and K. Kemp, Nucl. Instrum. Methods **116**, 487 (1973).

[14]K. Ishii, M. Kamiya, K. Sera, S. Morita, and H. Tawara, Phys. Rev. A **15**, 2126 (1977).

[15]T. Shibata, H. Ejiri, J. Chiba, S. Nagamiya, K. Nakai, R. Anholt, H. Bowman, J. Ingersoll, E. Rauscher, and J. O. Rasmussen, Nucl. Phys. **A308**, 513 (1978).

[16]D. Keefe, Annu. Rev. Nucl. Sci. **32**, 391 (1981).

[17]H. A. Bethe and E. E. Salpeter, *Quantum Mechanics of One- and Two-Electron Atoms* (Academic, New York, 1957).

[18]F. Sauter, Ann. Phys. (Leipzig) **9**, 217 (1931); **11**, 457 (1971).

[19]R. H. Pratt, A. Ron, and H. K. Tseng, Rev. Mod. Phys. **45**, 273 (1973).

[20]S. Hultberg, B. Nagel, and P. Olsson, Ark. Fys. **38**, 1 (1967).

[21]J. H. Scofield, University of California Report No. UCRL-51326, 1973 (unpublished). Some results are quoted in Ref. 19.

[22]F. Biggs, L. B. Mendelsohn, and J. B. Mann, At. Data Nucl. Data Tables **16**, 202 (1975).

[23]R. H. Pratt, Phys. Rev. **119**, 1619 (1960).

[24]R. D. Schmickley, Ph.D. thesis, Stanford University, 1966.

[25]H. W. Koch and J. W. Motz, Rev. Mod. Phys. **31**, 920 (1959).

[26]H. K. Tseng, R. H. Pratt, and C. M. Lee, Phys. Rev. A **19**, 187 (1979).

[27]J. D. Jackson, *Classical Electrodynamics* (Wiley, New York, 1962).

[28]W. A. McKinley and H. Feshbach, Phys. Rev. **74**, 1749 (1948).

[29]S. Ahlen, Rev. Mod. Phys. **52**, 140 (1980).

[30]C. M. Lee, L. Kissel, R. H. Pratt, and H. K. Tseng, Phys. Rev. A **13**, 1714 (1976).

[31]C. A. Quarles and D. B. Heroy, Phys. Rev. A **24**, 48 (1981).

[32]L. Kissel, C. A. Quarles, and R. H. Pratt, At. Data Nucl. Data Tables **28**, 381 (1983).